Plasmonic candle: towards efficient nanofocusing with channel plasmon polaritons

V S Volkov[1,5], **J Gosciniak**[1], **S I Bozhevolnyi**[1], **S G Rodrigo**[2], **L Martín-Moreno**[2], **F J García-Vidal**[3], **E Devaux**[4] **and T W Ebbesen**[4]

[1] Institute of Sensors, Signals and Electrotechnics (SENSE), University of Southern Denmark, Niels Bohrs Allé 1, DK-5230 Odense M, Denmark
[2] Instituto de Ciencia de Materiales de Aragón and Departamento de Física de la Materia Condensada, CSIC - Universidad de Zaragoza, E-50009 Zaragoza, Spain
[3] Departamento de Física Teórica de la Materia Condensada, Universidad Autónoma de Madrid, E-28049 Madrid, Spain
[4] ISIS, CNRS UMR 7006, Université Louis Pasteur, 8 allée Monge, BP 70028, 67083 Strasbourg, France
E-mail: vsv@sense.sdu.dk

Abstract. Channel plasmon polaritons (CPPs) propagating along the bottom of V-grooves cut into a metal were recently shown to exhibit strong confinement combined with low propagation loss, a feature that makes this guiding configuration very promising for the realization of ultracompact photonic components. Here, we present a comprehensive study of radiation nanofocusing with CCPs propagating along subwavelength metal grooves that are terminated with various types of tapers of different lengths. Tapered V-grooves are fabricated in a gold film using a focused ion beam milling technique, with the tapering being realized by gradually decreasing the groove width and/or depth (in different way for different structures), and characterized at telecom wavelengths with a collection scanning near-field optical microscope. Efficient CPP nanofocusing is directly demonstrated featuring a field intensity enhancement of up to ~130 for optimal taper configurations. Experimental

[5] Authors to whom any correspondence should be addressed.

IOP Institute of Physics ⏀ DEUTSCHE PHYSIKALISCHE GESELLSCHAFT

observations are found to be concurrent with three-dimensional finite-difference time-domain electromagnetic simulations, predicting the possibility of reaching an intensity enhancement of ∼1200 and opening thereby exciting perspectives for practical applications of CPP nanofocusing.

Contents

1. Introduction

Recent rapid developments in plasmonic circuitry [1] suggest abundant possibilities for further advancement towards practical realization of exciting optical phenomena associated with metal nanostructures. Thus, the phenomenon of nanoscale field confinement by surface plasmon (SP) manipulation has great potential to revolutionize many applications in nanophotonics ranging from quantum optics [2] to imaging [3], near-field optics [4, 5] and nanosensing [6]. A variety of SP focusing geometries has been suggested to achieve the high SP concentration on length scales smaller than the diffraction limit of light (in the surrounding dielectric), all supporting progressively stronger confined SP modes in the limit of infinitely small waveguide cross sections [7]–[14]. However, experimental demonstrations of SP nanofocusing [15, 16] have so far been indirect (based on far-field observations of scattered [15] or frequency upconverted [16] radiation) and inconclusive with respect to the field enhancement achieved in the focus. Recently, we have reported on the radiation nanofocusing with channel plasmon polaritons (CPPs) [17]–[19] that propagate along subwavelength metal grooves being tapered synchronously in depth and width. Efficient CPP nanofocusing at telecom wavelengths has been directly demonstrated with a scanning near-field optical microscope (SNOM), opening thereby exciting perspectives for practical applications of the CPP-based nanofocusing phenomenon. This first success encouraged us to further exploit the potential of CPP nanofocusing and to investigate intricate features of this exciting phenomenon in detail.

The idea of radiation (nano) focusing (and thereby greatly enhancing electromagnetic fields) by gradually decreasing a waveguide cross section has always been very appealing due to its apparent simplicity. Its realization, however, requires the corresponding waveguide mode to scale in size along with the waveguide cross section, a nontrivial characteristic that is not readily accessible and, for example, cannot be achieved with dielectric waveguides due to the diffraction limit. The physics of SP guiding is fundamentally different and intimately connected with the hybrid nature of SP modes, in which electromagnetic fields in dielectrics are coupled

to free electron oscillations in metals [20]. Several SP guiding configurations exhibit, in the limit of infinitely small waveguide dimensions, the required scale invariance, i.e. the mode size scaling linearly with that of the waveguide. The appropriate SP modes are supported, for example, by thin metal films (short-range SPs) and narrow gaps between metal surfaces (gap SPs), [21, 22] and by corresponding cylindrical, i.e. rod and coaxial, structures [23, 24]. Note that their nanofocusing [7]–[13] is conceptually simple only at a fairly basic level and requires dealing with several rather complicated issues, such as excitation of the proper SP mode [15] and balancing between SP propagation losses (that increase for smaller waveguide cross sections) and focusing effects [25, 26]. The situation becomes even more complicated if one considers SP modes whose scaling behavior is not straightforward. Thus CPP guides, which can be efficiently excited with optical fibers and used for ultracompact plasmonic components [19], exhibit rather complicated behavior with respect to their geometrical parameters [27, 28], and their potential for nanofocusing of radiation has not yet been totally explored.

Channel plasmons are SP modes that are bound to and propagate along the bottom of grooves cut into a metal [18, 29]. They were predicted to exhibit subwavelength transverse confinement, relatively low propagation loss [30] and single mode operation [27, 31] as well as efficient transmission around sharp bends [32]. To better understand the concept of CPPs let us first consider SP modes guided between two closely spaced metal surfaces so that SPs associated with individual metal surfaces become coupled. The dispersion equation for this guiding geometry is well known [33, 34] and its solution can be easily obtained, even when the metal dielectric function is complex. The main feature in this context is that, with the decrease of the slit width, the effective refractive index of a symmetric SP combination increases (while the propagation length decreases), starting from the value corresponding to the individual uncoupled SP [34]–[36]. Gap plasmons can be easily squeezed to subwavelength dimensions. Smaller gaps result in shorter-wavelength gap plasmons, although at the expense of greater propagation losses [34]. Because the mode field is nearly constant and close to its maximum for subwavelength gaps, however, the propagation loss determined by the portion of field penetrating the metal is as small as it can be for a given confinement. Let us now consider a straight groove cut into metal and having a V-shaped cross section. Light tends to concentrate in regions where its wavelength is shortest (i.e. where the effective refractive index is at maximum), ensuring plasmon field confinement at the bottom of the groove. It is important to note that the CPP guiding in V-grooves is counterintuitive: while a certain groove depth (for a given groove angle) is required to support a CPP mode, the CPP guiding approaches cut-off and the CPP mode field stretches farther out of the groove when the groove angle increases. Note that careful analysis of CPP waveguides requires elaborate and extensive numerical modeling [27], [30]–[32], but the design guidelines can be worked out using the effective index method (EIM) [35]–[37]. Within the framework of the EIM, one can find the CPP modes supported by a V-groove analyzing a one-dimensional (1D) layered (in depth) guiding structure, in which the top layer of air and the bottom layer of metal about a stack of layers having refractive indexes determined by the layer depth [37]. The normalized frequency of CPP waveguides can be obtained by integrating the index contrast over the groove depth that results in the following expression for the normalized waveguide parameter for CPP modes in V-grooves [28]

$$V_{\text{CPP}} \cong 2\sqrt{\frac{k_0 d_0 \varepsilon_0 \sqrt{|\varepsilon_{\text{d}} - \varepsilon_{\text{m}}|}}{|\varepsilon_{\text{m}}| \tan(\theta/2)}} \equiv 4d\sqrt{\frac{\pi \varepsilon_{\text{d}} \sqrt{|\varepsilon_{\text{d}} - \varepsilon_{\text{m}}|}}{\lambda w_0 |\varepsilon_{\text{m}}|}}, \tag{1}$$

where λ is the light wavelength ($k_0 = 2\pi/\lambda$), d_0 and w_0 are the V-groove depth and width, θ is the groove angle so that $\tan(\theta/2) = 0.5 w_0/d_0$, ε_d and ε_m are the dielectric constants of the dielectric and the metal, respectively. The concept of normalized waveguide parameter (normalized frequency) is not new and was previously used for planar thin-film waveguides [38] as a basic parameter that along with the asymmetry parameter allowed charting universal dispersion curves for TE modes. Note that a formal justification of the waveguide parameter (introduced in [28] by use of effective index approach) has been recently provided by use of an *analytic* description of V-grooves [39]. It has been demonstrated [28, 39] that V-grooves with different dimensions and operating at different wavelengths but having the same parameter V_{CPP} feature very similar field confinement. With this in mind, we came up with the idea of CPP nanofocusing by gradually decreasing the groove depth while synchronously decreasing its angle so that the corresponding waveguide parameter (equation (1)) would be kept constant. In this case (and within the same approximation [28]), one can show that the CPP effective index of nanometer-sized V-grooves diverges toward the taper end: $N_{CPP} \sim (k_0 d_0)^{-1}$; i.e. it behaves in the same manner as that of the SP mode of a tapered nanowire [10]. In the adiabatic approximation, the CPP field is continuously squeezed by walls of a tapered V-groove with the maximum field being limited only by the CPP propagation loss. In general, similarly to the nanofocusing with nanowires [25, 26], the field enhancement at the taper end is a result of the interplay between CPP dissipation (contributed to by CPP absorption, reflection and out-of-plane scattering) and field squeezing.

This paper is organized as follows: in section 2, the experimental arrangement and the sample used is described. Section 3 is devoted to the experimental results featuring the SNOM images obtained at different CPP tapered structures and their interpretation. Section 4 presents results of 3D-finite-difference time-domain (FDTD) simulations of CPP nanofocusing at telecom. Finally, our conclusions are offered in section 5.

2. Experimental arrangement

For the experimental verification of our idea, we have fabricated, using focused ion beam (FIB) milling, in a $1.8\,\mu$m thick gold layer (deposited on a glass substrate coated with indium tin oxide) several straight $150\,\mu$m long V-grooves with the angles close to $28°$ and depths of 1.1–$1.3\,\mu$m, which were gradually tapered out over different distances ($t = 2, 3, 4, 6, 7$ and $13\,\mu$m). The fabricated sample contained three types of V-groove tapers:

- V_{CPP}-constant groove tapers (VCGTs), which are the same as those used in our previous experiments with CPP nanofocusing [17]. The tapering was realized by decreasing, gradually and linearly with respect to the length of the tapered part, the number of pixels representing the groove width in the taper region while maintaining the dwell time (time of exposure of on pixel). Making cross cuts with the FIB, we have checked that such a milling procedure results indeed in simultaneous decreasing the groove depth and angle (figure 1(c)).

- Angle-constant groove tapers (ACGTs), for which the number of pixels (V-groove width) and the dwell time (V-groove depth) were reduced simultaneously, with the angle near the groove bottom being kept constant (figure 2(a)).

- Width-constant groove tapers (WCGTs), where the dwell time was reduced continuously with the groove width being constant (figure 2(b)). Essentially, in this case V-grooves are tapered only in 1D (in depth).
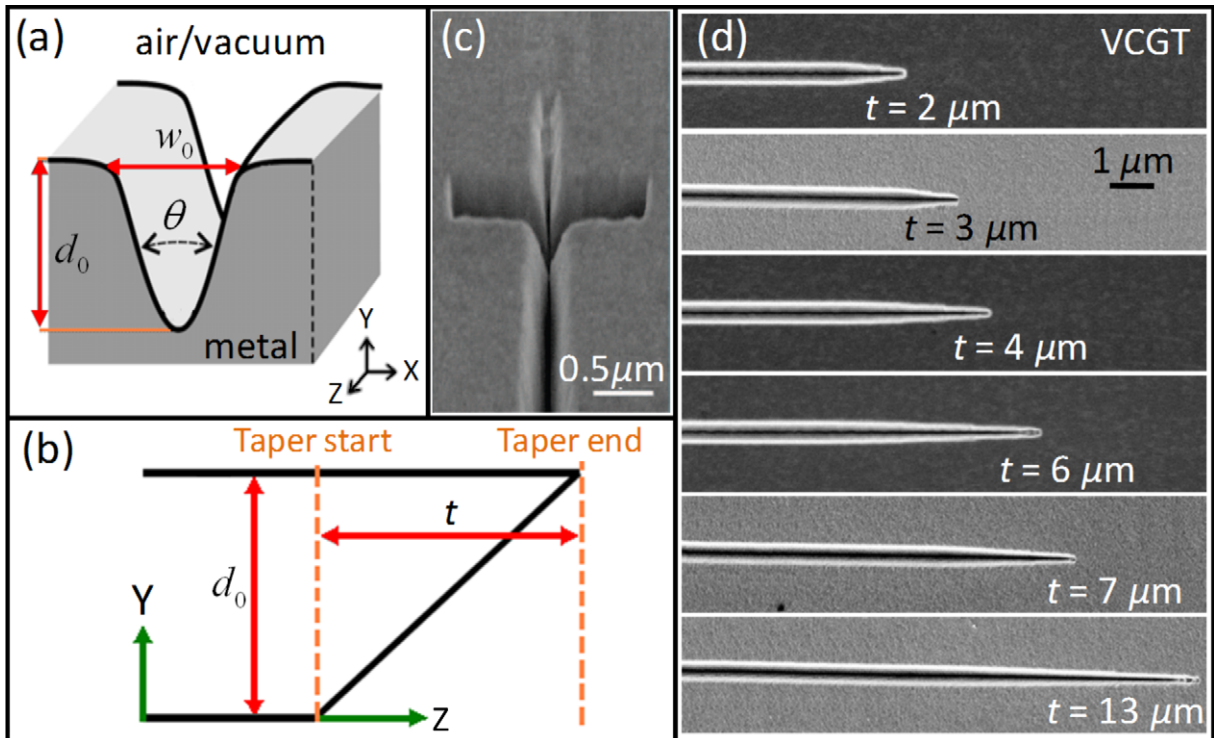
IOP Institute of Physics ⏀ DEUTSCHE PHYSIKALISCHE GESELLSCHAFT

Figure 1. VCGTs: (a) schematic of the V-groove geometry and (b) the taper region. (c) SEM image of a VCGT cut in the taper region to reveal a decrease in the groove angle toward the taper end. (d) SEM images of fabricated tapered V-grooves having different taper lengths: 2, 3, 4, 6, 7 and 13 μm.
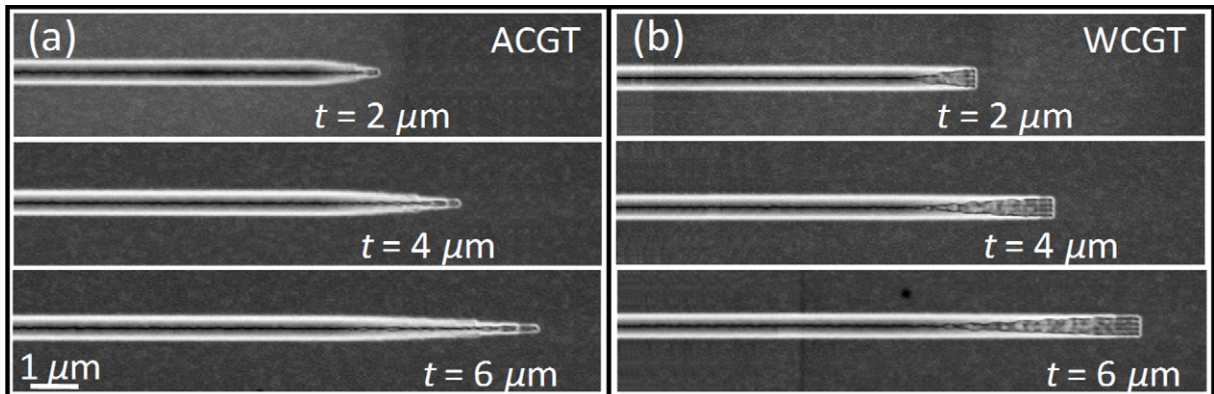

Figure 2. Tapered V-grooves: ACGTs and WCGTs. (a) SEM images of ACGTs of different lengths: 2, 4 and 6 μm. To fabricate these structures the number of pixels and the dwell time were reduced simultaneously, with the angle near the groove bottom being kept constant. (b) SEM images of WCGTs of different lengths: 2, 4 and 6 μm. To fabricate these structures the dwell time was reduced continuously with the groove width being kept constant. So, in this case the final structures are tapered only in depth.
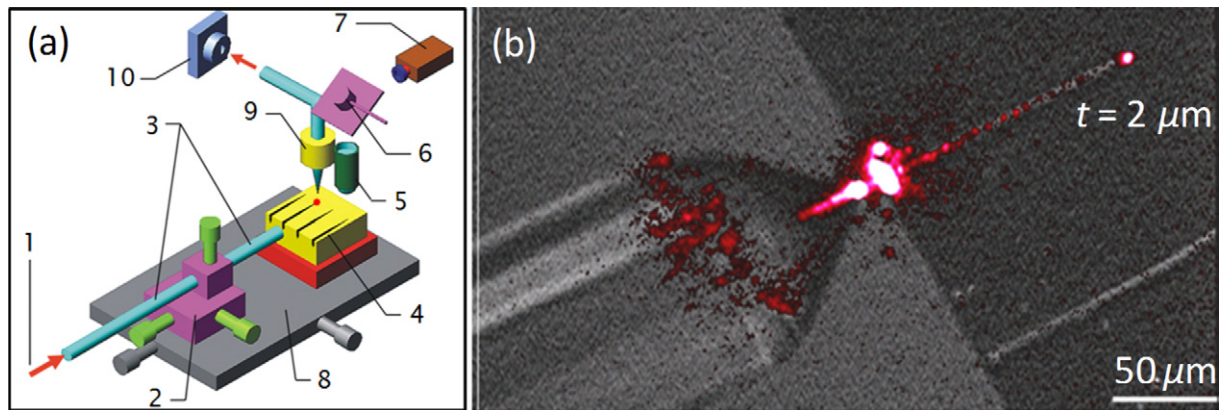
Figure 3. Experimental arrangement. (a) Schematic layout of the experimental setup: (1) TE-polarized radiation (the electric field is parallel to the sample surface plane) from tunable laser (1430–1620 nm); (2) 3D: X, Y, Z stage; (3) in-coupling tapered-lensed polarization-maintaining single-mode fiber; (4) sample: gold film containing several V-groove tapers; (5) microscope objective of 20 times magnification; (6) mirror; (7) IR camera; (8) 2D: X, Y stage; (9) SNOM operated in collection mod; (10) InGaAs photoreceiver. (b) Microscope image of a coupling arrangement superimposed with the far-field image taken at the excitation wavelength $\lambda \approx 1480$ nm with an infrared camera, showing the track of CPP propagation and a bright spot at the 2 μm long taper.

The experimental setup employed for the characterization of the fabricated structures is essentially the same as that used in our previous experiments with photonic crystal waveguide structures [40]. It consists of a collection SNOM with an uncoated sharp fiber tip used as a probe and an arrangement for launching tunable (1430–1620 nm) TE/TM-polarized radiation into a metal groove by positioning a tapered-lensed polarization-maintaining single-mode fiber (figure 3). Note, that since the main component of the SPP electric field is oriented perpendicular to the metal surface [20], the CPP electric field tends to be oriented perpendicular to the groove walls and thereby, for small groove angles, parallel to the sample surface plane. The adjustment of the in-coupling fiber with respect to the illuminated V-groove channel was accomplished when monitoring the SPP propagation along the sample surface with the help of a far-field microscopic arrangement. The track of the propagating radiation (distinguishable for all structures and wavelengths) featured, apart from a gradual decay in visibility with the propagation distance, a rather bright spot at its termination (figure 3(b)). These far-field observations have also confirmed the expected polarization properties of the guided radiation [35] and demonstrated its (relatively) low dissipation. Following these experiments (that include also adjusting the in-coupling fiber position to maximize the coupling efficiency) we moved the whole fiber-sample arrangement under the SNOM head and mapped the intensity distribution near the surface of the groove with an uncoated sharp fiber tip of the SNOM. The near-field optical probe used in the experiment has been produced from a single-mode silica fiber by ∼120 min etching of a cleaved fiber in 40% hydrofluoric acid with a protective layer of olive oil. The resulting fiber tip has a cone-angle of ∼30° and curvature radius of less than 90 nm. The tip was scanned along the sample surface at a constant distance of a few nanometers

maintained by shear force feedback. It should be borne in mind that this distance could not be maintained in the middle of the groove (given the groove dimensions and the tip size), a circumstance that might influence the characterization of CPP mode cross section. Near-field radiation scattered by the tip was partially collected by the fiber itself and propagated in the form of the fiber modes towards the other end of the fiber, where it was detected by a femtowatt InGaAs photo receiver.

3. Experimental results

All fabricated plasmonic tapers were excited at different wavelengths ranging from 1430 to 1620 nm with TE-polarized light and imaged with SNOM. Topographical and near-field optical images of efficient CPP guiding by fabricated V-grooves were recorded at the distance of $\sim$120 μm from the in-coupling groove edge (to decrease the influence of the stray light., i.e. the light that was not coupled into the CPP mode) and in the whole range of laser tunability. The appearance of the optical images is similar to those obtained with photonic crystal waveguides [40] featuring efficient mode confinement (in the lateral cross section) at the grooves and intensity variations along the propagation direction. The latter can be most probably accounted for by the interference between the CPP modes incident and reflected from the tapers as well as scattered field components (including stray light [35]). Despite the aforementioned signal variations, it has been found that in the wavelength range of 1430–1620 nm, the full-width at half-maximum (FWHM) of the CPP mode is practically constant ($0.7 \pm 0.1 \mu$m). We have also found that the signal does not go to zero outside the groove indicating the presence of a homogeneous background at the level of $\sim$15% compared to the maximum signal (inside the groove). Note that this background signal is also present in the optical images recorded in constant plane mode at different heights up to 600 nm above the sample surface. However, it is not clear to what extent it influences the signal measured in the middle of a V-groove with the SNOM fiber tip being actually below the sample surface by $\sim$40–100 nm, depending on the SNOM fiber tip shape. Considering the fabricated grooves parameters ($\theta \sim 28°$ and $d_0 \sim 1.1$–1.3 μm), it is expected that the fundamental CPP mode can be quite close to cut-off [35, 39], with the CPP field extending out of the groove. The latter would facilitate its observation both with a far-field microscope (weakly confined mode is easier to scatter by surface features) and the SNOM (the detection efficiency of a fiber probe increases for lower spatial frequencies [41]). Finally, it should be noted that the SNOM images presented here (figures 4–10) are oriented in such a way that the CPP propagates from left to right (in the horizontal direction).

3.1. SNOM measurements of VCGTs

Our SNOM investigations showed that all fabricated VCGTs exhibited the effect of signal enhancement at the taper end, with the near-field optical images featuring subwavelength-sized bright spots located at the taper end as judged from the (simultaneously recorded) topographical images. The evolution of the near-field intensity distribution inside the channels with the increase of the taper length is shown in figures 4 and 5 for the wavelength of 1480 nm. These figures demonstrate topographical and corresponding near-field optical images exhibiting typical features (e.g. efficient and well-confined CPP guiding, clearly noticeable optical signal modulations etc) appearing also on the images recorded at other wavelengths. Note that the
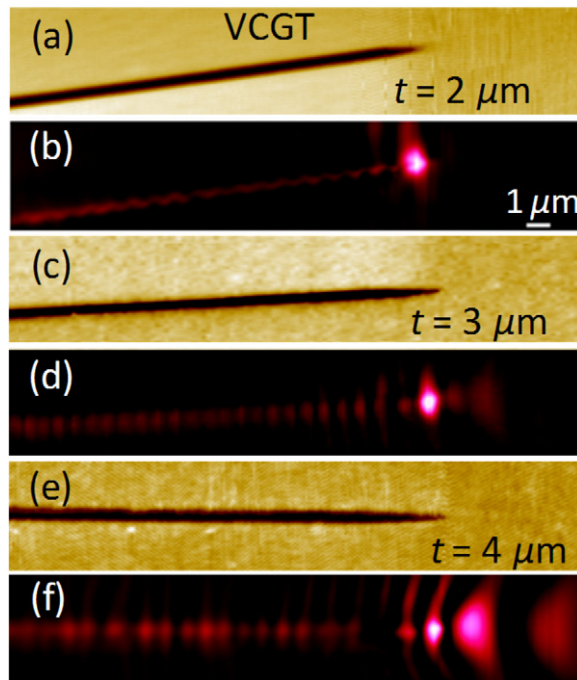
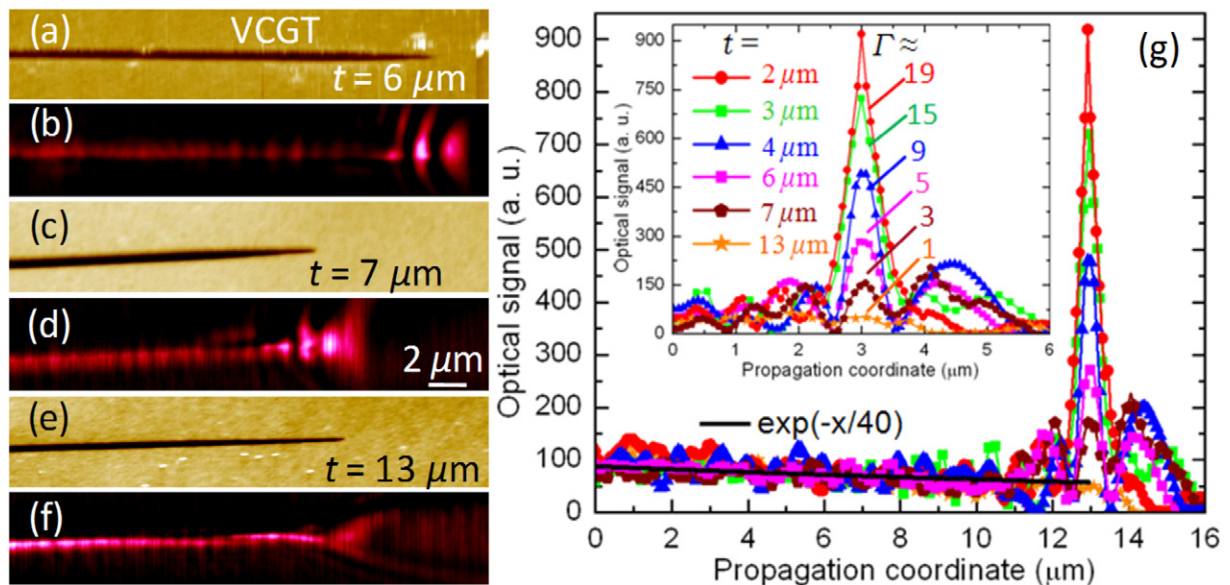**IOP** Institute of Physics Φ DEUTSCHE PHYSIKALISCHE GESELLSCHAFT

Figure 4. Plasmonic candle. Pseudo-color (a, c, e) topographical and (b, d, f) near-field optical images of VCGTs of different lengths: (a, b) 2 μm, (c, d) 3 μm and (e, f) 4 μm. SNOM images taken at $\lambda \approx 1480$ nm with shear-force feedback.

Figure 5. Plasmonic candle. Pseudo-color (a, c, e) topographical and (b, d, f) near-field optical images of VCGTs of different lengths: (a, b) 6 μm, (c, d) 7 μm and (e, f) 13 μm. All SNOM images taken at $\lambda \approx 1480$ nm with shear-force feedback. (g) Normalized cross sections obtained with optical images (shown in figures 4 and 5) recorded for the tapered V-grooves with different taper lengths.

most remarkable enhancement effect was observed (independently of the wavelength) for the 2 and 3 μm long tapers (figures 4(b) and (d)). This effect gradually deteriorated for the longer tapers and practically vanished for the 13 μm long taper (figure 5(f)). Let us now discuss the results obtained with the measured tapers in more detail. With the smallest length of the taper (2 μm), we have observed an efficient CPP focusing to a confined spot with the FWHM being in this case $\approx 0.5\,\mu$m. Note that the spot size is considerably smaller than the wavelength used. It has been found that with the increase of the taper length the intensity of the bright spot is dropped down with the CPP starting to be scattered (the optical signal diverging after the taper end seen from the SNOM images). We believe that the optimum taper length (2 μm) is the main parameter responsible for the efficient CPP focusing with VCGTs. This optimum length is directly related to constructive interference of the propagating (toward the taper) and reflected CPP modes, though it is affected by the CPP propagation loss as well. Using the exponential fit to the optical signal variation along the CPP propagation for different VCGTs excited at $\lambda \approx 1480$ nm, we evaluated the CPP propagation length of $\sim 40\,\mu$m, which is consistent with the previous observations [19], and the signal enhancement Γ defined as the ratio between the maximum signal and that expected to be at the taper end coordinate in its absence (figure 5(g)). We should emphasize that the relationship between near-field optical signal distributions and field intensity distributions existing near the sample surface (in the absence of a SNOM probe) is very complicated [42]. Even in a very simple approximation of the dipole-like detection (taking place at the position of an effective detection point inside a fiber probe) [41], different field components contribute differently to the detected signal, making it impossible to directly relate the near-field intensity distributions and the corresponding SNOM images. In this situation, it is extremely important to control that the detected signal does originate from the evanescent field components (and thereby is associated with the focused CPP fields), since the detection of propagating waves, such as scattered at the taper, is much more efficient than that of evanescent ones [41, 42]. Near-field optical images were recorded with shear force feedback, a few nanometers away from the surface, and then with the SNOM fiber probe scanning along planes located ~ 100 and 300 nm from the sample surface (figure 6). A drastic signal decrease and significant image blurring observed with the increase of the probe–surface distance signify unambiguously that the bright spots seen on the SNOM images are indeed the result of detection of evanescent (CPP) field components. It is further seen (e.g. for the 2 μm long taper) that with the increase of the SNOM tip–surface distance up to only 100 nm the maximum optical signal (at the bright spot) decreased by a factor of ~ 6 (cf figure 6, panels (b) and (c)) while the CPP-related signal measured away from the taper region decreased only by a factor of ~ 2. For larger tip–surface distances (≈ 300 nm), the image appearance deteriorated significantly, and the signal decrease slowed, reaching a background value of ~ 15% compared to the CPP signal inside the groove (figure 6(d)). With this in mind, it is reasonable to assume that, in both cases, the optical signals being proportional to the field intensity (at an effective detection point [41]) decrease exponentially with the probe–surface distance but at different rates, because the corresponding optical fields are laterally confined to the different widths. The latter implies that the observed intensity enhancement decreases also exponentially with the height of the observation plane. Finally, taking into account the aforementioned background level of the detected CPP signal and the circumstance that the effective detection point is located typically ~ 150 nm away from the uncoated SNOM tip end [41], we have obtained significant field intensity enhancements (~ 130 and ~ 55) realized at the sample surface with the 2 and 3 μm long VCGTs, respectively.
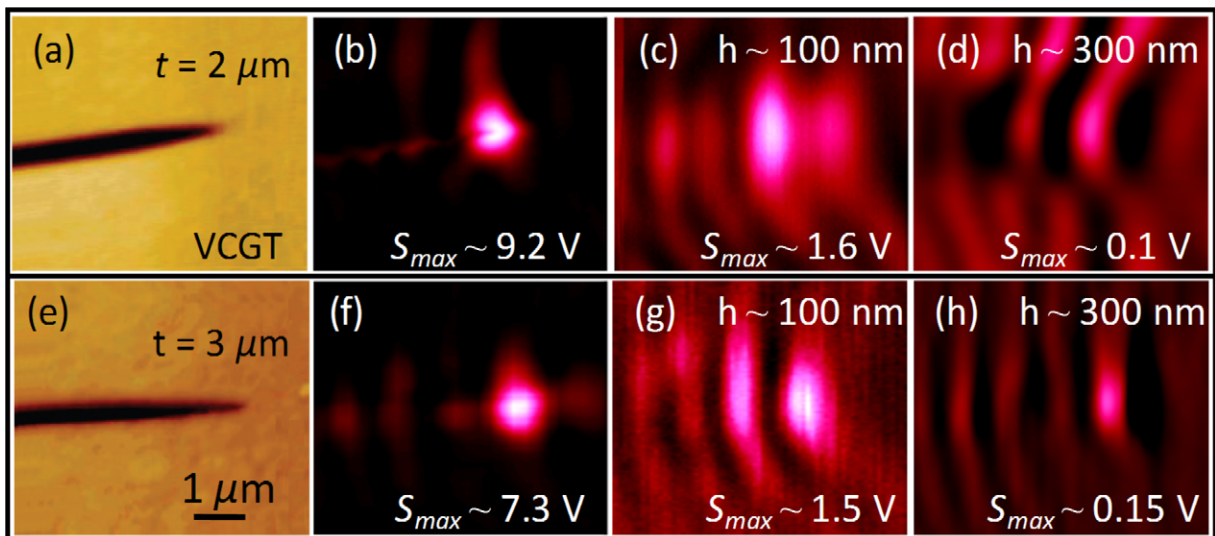
Figure 6. Plasmonic candle: influence of evanescent field components. Pseudo-color (a, e) topographical and near-field optical ($\lambda \approx 1480$) images taken (b, f) with shear force feedback and (c, g) at 100 and (d, h) 300 nm distances from the sample surface with the tapered V-grooves having different taper lengths: (a-d) 2 and (e)–(h) 3 μm. The decrease in signal and the significant image blurring when increasing the probe-surface distance reveal the dominance of the evanescent field components in the images obtained.

3.2. SNOM measurements of ACGTs

Similar SNOM investigations were also carried out with angle-constant tapers of different lengths: 2, 4 and 6 μm. The typical SNOM images obtained at $\lambda \approx 1480$ nm are shown in figure 7. From these results one can clearly see that the near-field optical image recorded for the shortest taper ($t = 2\,\mu$m) features a clearly pronounced subwavelength-sized bright spot (characterized by the FWHM $\approx 0.7\,\mu$m and $\Gamma \sim 10$) located at the taper end (figure 7(b)). The brightness and shape of the spot were found to be strongly dependent on the length of the tapered structure. Thus, one can see that the spot significantly deteriorated for the 4 μm long taper (figure 7(d)) by spreading in lateral cross section (along with signal diverging after the taper end which also presents at figure 7(f)) and practically vanished for the 6 μm long taper (figure 7(f)). High resolution near-field optical images obtained at $\lambda \approx 1480$ nm for the 2 μm long ACGT (featuring the best spot) at different tip–surface distances are shown in figure 8. It is seen that the images retained the appearance not only when changing from shear-force feedback mode to constant height mode (indicating the absence of topographical artifacts) but when further increasing the tip–surface distance to ~ 600 nm. The average CPP-related signal measured within the V-groove area (away from the taper region) was found to decrease rapidly (by a factor of ~ 2) as the tip–surface distance increases to only ~ 100 nm above the sample surface. One can see that the image become blurred (figure 8(c)) exhibiting low-contrast signal variations, confirming that the main contribution to the CPP signal detected at the groove originated indeed from the CPP (evanescent) field. At the same time, we have found that the maximum optical signal (at the bright spot) did not change noticeably with increase of the tip–surface distance up
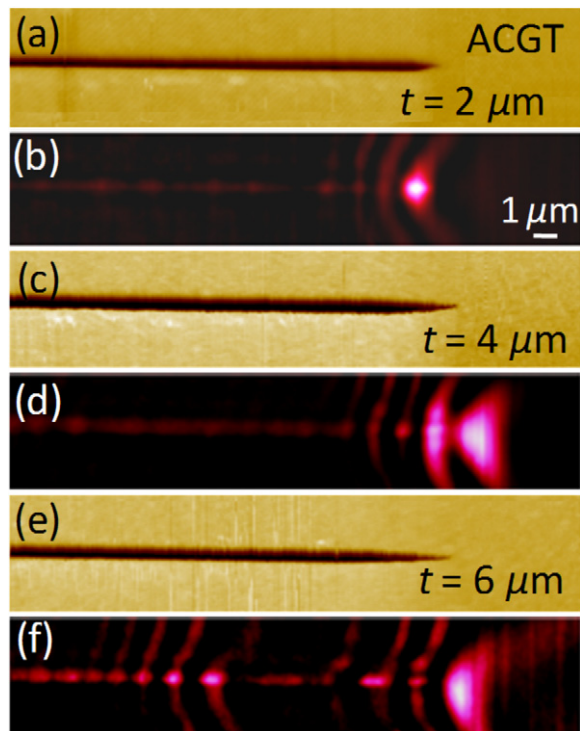
Figure 7. Pseudo-color (a, c, e) topographical and (b, d, f) near-field optical images of ACGTs of different lengths: (a, b) 2 μm, (c, d) 4 μm and (e, f) 6 μm. SNOM images taken at $\lambda \approx 1480$ nm with shear-force feedback.

to ~100 nm and became even slightly higher than that detected in shear-force. For even larger tip–surface distances (up to ~600 nm) the maximum optical signal detected from the bright spot decreased inconsiderably having the signal level of ~96% from the maximum optical signal recorded at the surface (cf figure 8, panels (b) and (d)). These observations *directly* confirm that, for this ACGT configuration (with $t = 2\,\mu$m), the field components scattered by the taper end and propagating out of the surface plane contributed much stronger the process of SNOM images formation when compared to evanescent CPP fields detected away from the taper region. The explanation for this interesting phenomenon should be directly related to the geometry of the investigated taper. The tapering in this case is realized by simultaneously decreasing the groove width and depth in the taper region (gradually and linearly with respect to the length of the taper), with the angle near the groove bottom being kept constant. This means that as the taper end is approached (and $V_{CPP} \rightarrow 0$ [17]) the depth of the V-groove approaches quickly a certain cut-off value (with the CPP mode index N_{CPP} being approaching to that in air), below which no CPP mode could be found inside the V-groove [36, 37]. For such a critical groove depth the CPP mode field starts to be progressively extended (scattered) outside the groove. Together with the simultaneous strong CPP mode squeezing in the lateral cross section (with the decrease in the groove width) it produces a spot which is strongly confined in the surface plane and positioned very close to the taper end. Note that such a nicely confined source of scattered field components can only be realized for very short taper lengths ($t = 2\,\mu$m or even shorter that that). For longer tapers CPP mode field leaks out of the groove before it approaches the taper end where CPP can be efficiently squeezed in width (creating a bright spot).
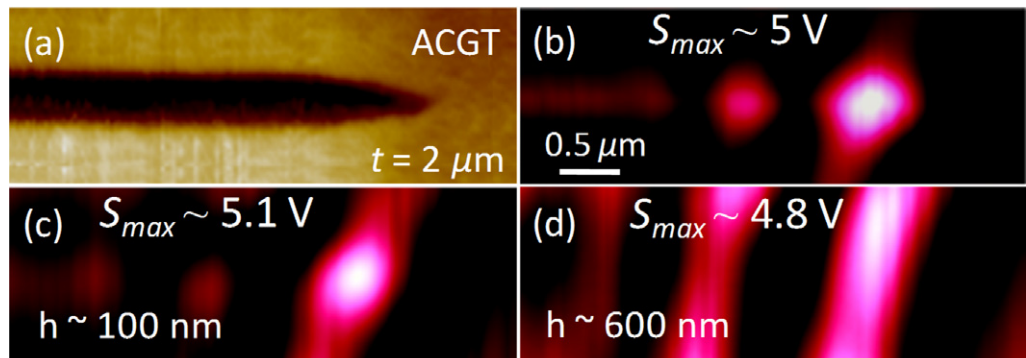
Figure 8. ACGT ($t = 2\,\mu$m): influence of evanescent field components. Pseudo-color (a) topographical and (b)–(d) near-field optical ($\lambda \approx 1480$ nm) images taken (b) with shear-force feedback and at (c) 100 and (d) 600 nm distances from the sample surface.

3.3. SNOM measurements of WCGTs

Finally, we have performed SNOM characterization of the WCGTs. The typical SNOM images obtained at $\lambda \approx 1480$ nm (for the structures of different lengths) are shown in figure 9. The near-field optical image recorded for the shortest structure ($t = 2\,\mu$m) features a clearly pronounced bright spot located close to the end of the taper (figure 9(b)). The brightness (and shape) of the spot were found to be strongly dependent on the length of WCGT with the spot being rapidly deteriorated for the $4\,\mu$m long taper and practically vanished for the $6\,\mu$m long taper (figure 9(f)). Note that the bright spot produced by $2\,\mu$m long WCGT is significantly wider (FWHM $\approx 1\,\mu$m) than those observed with VCGTs and ACGTs of the same lengths. This observation was not surprising. WCGTs were fabricated by continuously reducing the depth of the V-grooves with the groove width being kept constant and the final structures were only tapered in depth. So, with the decrease of the groove depth the CPP mode (propagating to the end of the WCGT) starts to be progressively extended outside the groove as soon as the depth of the V-groove approaches the cut-off value. Since the propagating CPP mode field is not squeezed in lateral dimension (the width of the taper is constant) the bright spot appeared (due to the scattering process) at the end of the $2\,\mu$m long WCGT is significantly wider than those observed with different types of tapered structures. We have also directly investigated the process of CPP scattering (by $2\,\mu$m long WCGT) and optical signal propagation away from the sample surface plane by recording the optical images at different SNOM tip–surface distances (figure 10). It was found that, with the increase of the tip–surface distance up to $\sim$200 nm (figure 10(c)) the bright spot became wider with the maximum optical signal being at the same level as the shear-force optical signal. For even larger tip–surface distances (up to $\sim$600 nm), the optical images changed inconsiderably having the optical signal level of $\sim$90% from the maximum signal recorded at the surface (figure 10(d)). The features observed indicate that $2\,\mu$m long WCGT efficiently converts the evanescent CPP mode field into the scattered field components propagating into the out-of-plane direction. These findings also suggest the possibility of the inverse transformation i.e. efficient coupling of focused (e.g. by use of optical objective) and properly polarized optical radiation into the CPP mode with the groove taper of this kind.
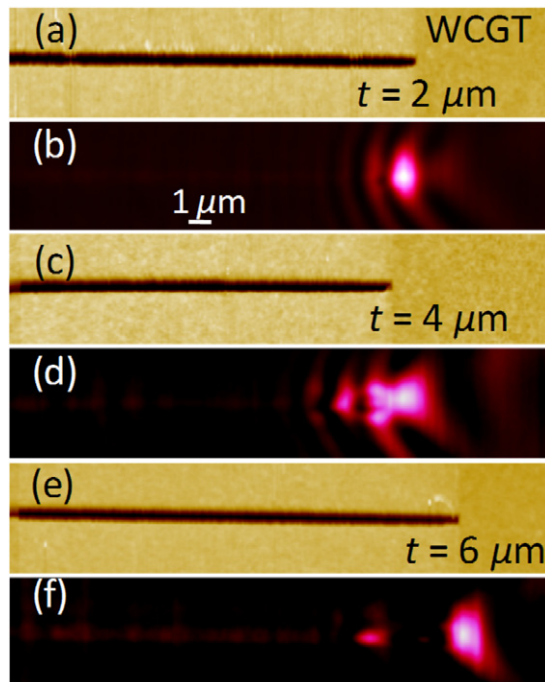
Figure 9. WCGTs. Pseudo-color (a, c, e) topographical and (b, d, f) near-field optical images of WCGTs of different lengths: (a, b) $2\,\mu$m, (c, d) $4\,\mu$m and (e, f) $6\,\mu$m. SNOM images taken at $\lambda \approx 1480$ nm with shear-force feedback.
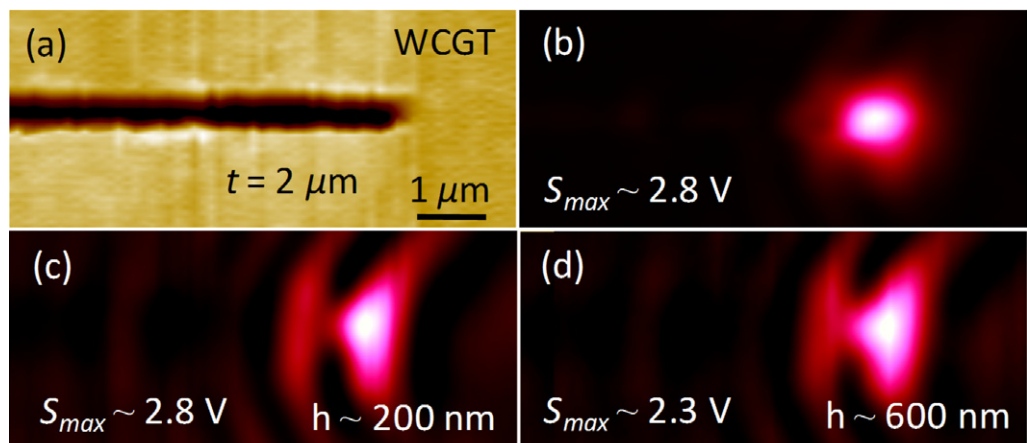

Figure 10. WCGT ($t = 2\,\mu$m): influence of evanescent field components. Pseudo-color (a) topographical and (b, c, d) near-field optical ($\lambda \approx 1480$) images taken (b) with shear-force feedback and (c, d) at 200 and 600 nm distances from the sample surface.

3.4. Determination of the CPP field enhancement

The SNOM images recorded at different tip–surface distances allowed us to determine the CPP field enhancement (in the close proximity to the surface) for the different types of $2\,\mu$m long tapers. As already mentioned, the relationship between near-field optical signal distributions
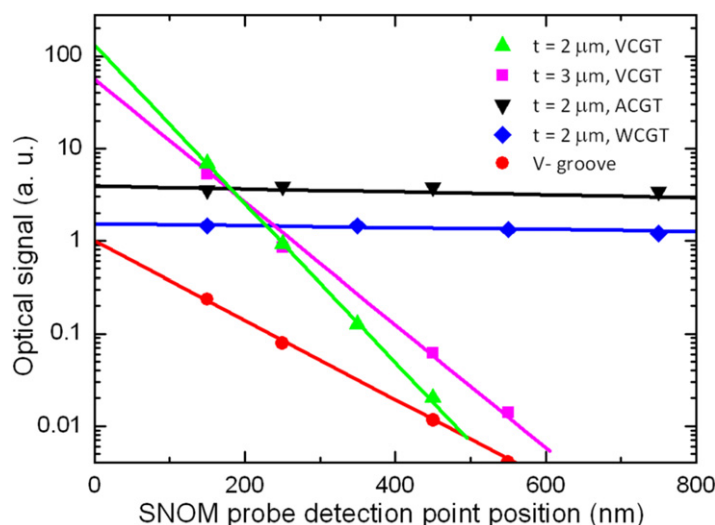
Figure 11. Dependences of the CPP field enhancement on the position of the SNOM efficient detection point with respect to the distance from the surface—measured (symbols) from the experimental SNOM images and fitted (solid lines) with the linear fit. The optical background has been extracted from all corresponding SNOM images and received optical data were normalized to the maximum optical signal in V-groove (away from the taper region).

(recorded with the SNOM) and field intensity distributions existing near the sample surface (in the absence of a SNOM probe) is very complicated [42]. In order to simplify it to a certain level, one can use a rather simple approximation of the dipole-like detection which takes place at the position of an effective detection point inside a fiber probe. The position of this efficient detection point is fully dependent on the probe tip parameters—the size, shape and the apex angle of the fiber tip. Therefore, the quality of the SNOM fiber probe is of great importance and the probe tip shows itself as the most important part of the microscope. Our previous extensive (both experimental and theoretical) investigations of the SNOM fiber tip detection efficiency allowed us to develop a simple, rational and sufficiently reliable way of characterization of fiber probes used in our experiments [41]. Thus, it has been found that for the fiber tip (with apex angle of $\sim 30°$) used in our SNOM experiments the effective detection point is found to be located (inside the SNOM probe) ~ 150 nm away from the fiber tip. This is a constant distance which is always kept between the tip detecting point and the scanning surface when SNOM is operated in shear-force mode. With this in mind, we have plotted values of the maximum optical signal taken from corresponding SNOM images (recorded at various tip–surface distances for the different types of 2 μm long tapers) as a function of the SNOM tip detection point position (figure 11). The corresponding optical signal values (presented on the plot) were directly obtained from different parts of SNOM images: from the bright spots (near the tapers ends) and from the V-groove regions (away from the taper region). The optical signal values (being proportional to the field intensity) were plotted on a logarithmic scale and found to be decreased exponentially with the increase of the probe-surface distance. These signal-to-distance dependences were linearly fitted with solid lines in order to determine the CPP field enhancement at zero position of the detecting point (that corresponds to direct contact with

the surface). Finally, taking into account the aforementioned background level of the detected CPP signal (and subtracting this background from the corresponding SNOM images) we have obtained significant CPP field intensity enhancements ($\sim$130 and $\sim$55) realized at the sample surface (at $\lambda \approx 1480$) with the $2\,\mu$m and $3\,\mu$m long VCGTs, respectively. Much weaker CPP field intensity enhancements (~ 4 and $\sim$1.6) were induced at this wavelength for $2\,\mu$m long ACGTs and WCGTs that has clearly demonstrated the weakness of these tapering geometries for efficient CPP nanofocusing.

4. 3D-FDTD simulations

In order to gain further insight and reveal the potential of CPP nanofocusing, we have conducted 3D-FDTD simulations for V-grooves terminated with $2\,\mu$m long tapers. In the considered case of the CPP-based nanofocusing structure the gold metal surface is deforming from the straight channel geometry to a flat geometry in a continuous way along the mode propagation direction i.e. along the Z-axis (figure 1(b)). In other words, the channel parameters (being kept constant) become functions of the z-coordinate. We have considered linear tapering with respect to the groove depth: $d(z) = d_0\{1 - (z - z_0)/t\}$, where t is the taper length, z_0 is the starting coordinate of the taper, and $z_0 < z < z_0 + t$. All structures have an initial section with constant channel depth ($d_0 = 1\,\mu$m), width ($w_0 = 450$ nm) and constant angle ($\theta = 28°$) up to $z = 2\,\mu$m. The groove width in a taper region is adjusted following four different dependences: $w(z) = w_0(d(z)/d_0)^n$, $n = 0, 1, 2$ and 3. Consequently, the normalized waveguide parameter introduced in equation (1) varied as follows: $V_{CPP}(z) = V_{CPP}^0 \{d_0/d(z)\}^{0.5n-1}$, so as the taper tip is approached, the parameter V_{CPP} was maintained constant for $n = 2$, while $V_{CPP} \to 0$ for $n = 0$ (that corresponds to the width-constant groove tapering procedure), $V_{CPP} \to 0$ for $n = 1$ (constant-angle groove tapering) and $V_{CPP} \to \infty$ for $n = 3$ (the last one cannot be realized experimentally). In the FDTD method Maxwell's equations are discretized in both space and time [43]. The resulting finite-difference equations are solved in a leapfrog manner: the electric field vector components in a volume of space are solved at a given instant in time; then the magnetic field vector components in the same spatial volume are solved at the next instant of time; and the process is repeated over and over until the desired transient or steady-state electromagnetic field behavior is fully evolved. Therefore, convergence depends on both mesh size and temporal step. In order to properly calculate the influence of material properties, the rapidly decaying fields inside the metal should be accurately computed. We have used the 'piece linear recursive convolution method' [43], which can efficiently treat dispersive media, provided their dielectric $\varepsilon(\omega)$ constant can be expressed as a sum of Drude and Lorentz terms. The tight confinement of the mode requires very fine meshes (we used a mesh of 10 nm). The simulation domain is a parallelepiped surrounded by perfect matched layers (PMLs) to avoid spurious reflections on the system boundaries. The fundamental CPP mode is excited by a monochromatic oscillating magnetic dipole source pointing along the Z direction and located at $z = 0$ into the channel. Such a light source has the same E-field symmetry of a CPP, so it efficiently couples to CPPs. The excitation wavelength is chosen to be 1480 nm. Near-field information can be readily retrieved once the stationary state is reached.

The best (with respect to the field enhancement achieved at the taper end) performance for the optimum taper length ($t = 2\,\mu$m) was found for $n = 2$ as expected (figure 12(a)). The theoretical findings agree well with our qualitative considerations in the sense that the groove tapering should be conducted so that the groove depth and width decrease in accord keeping the
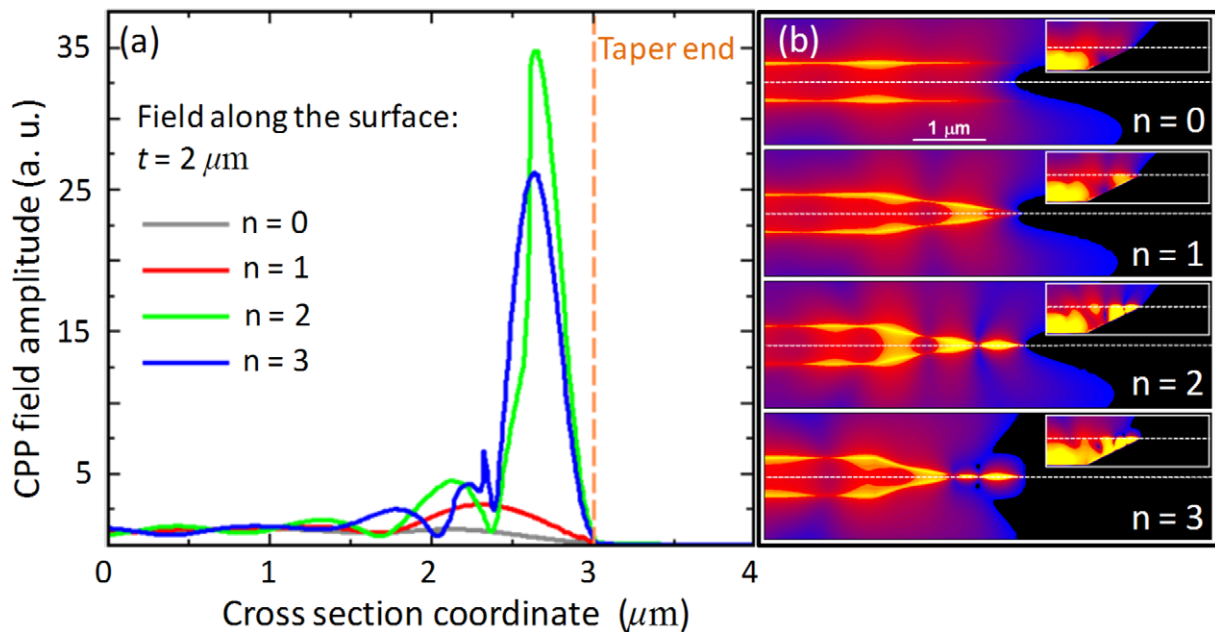
Figure 12. 3D-FDTD simulations of CPP nanofocusing at 1480 nm wavelength: (a) The figure depicts cross sections of the field amplitude distributions along the dashed lines shown in (b), which renders field magnitude distributions in the sample surface plane ($\sim$10 nm over the surface) for the 2 μm long taper. The groove width and depth decrease in accordance with the dependence described by $n = 0; 1; 2; 3$ (see text). Each inset in (b) shows the corresponding near-field maps at $x = 0$ lateral cross section.

normalized CPP parameter (equation (1)) constant. The simulation results are also consistent with the experimental observations, which feature the strongest enhancement for the 2 μm long VCGT (that corresponds to $n = 2$) and the occurrence of a very bright spot in near-field optical images (cf figures 6 and 12). We believe that the estimated optimum taper length is mainly related to constructive interference of the propagating (toward the taper) and reflected CPP modes, though it is affected by the CPP propagation loss as well. To verify this, we also performed electromagnetic simulations of corresponding near-field signal distributions (i.e. $x = 0$ lateral cross sections with size: $8.5 \times 2 \mu m^2$) of CPP propagation and focusing with the 2 μm long tapers in which the grooves width and depth was decreased in accordance with different dependences described with $n = 0, 1, 2$ and 3 (figure 13). These simulations showed the increase of the standing wave pattern contrast for the taper with $n = 2$ (that is obviously related to a corresponding increase of the reflection efficiency of the taper) as well as a strong scattering in the taper region (especially for $n = 0$ and 1), which is in good agreement with our experimental data (cf figures 8, 10 and 13(a) and (c)). However, the simulated V-groove taper (with optimum parameters: $t = 2 \mu m$, $n = 2$) characteristics are much better with respect to the field enhancement than those estimated from our experimental SNOM images (see figure 11). Indeed, using the same definition as before one obtains the field intensity enhancement of $\sim$1200 for the 2 μm long taper with $n = 2$ (figure 12(a)). On the other hand, some difference should be expected given the limited FIB resolution and the fact that the maximum field intensity is calculated to be fairly close to the taper end with the taper width being only $\sim$50 nm (while
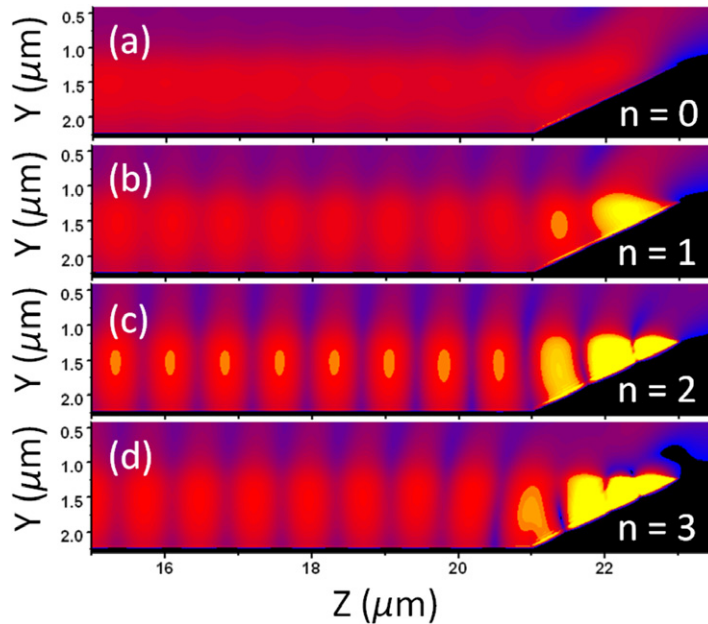
IOP Institute of Physics **Φ** DEUTSCHE PHYSIKALISCHE GESELLSCHAFT

Figure 13. 3D-FDTD simulations of CPP field magnitude distributions calculating for $2\,\mu$m long tapers in which the groove width and depth decrease in accordance with different dependences described with $n =$ (a) 0, (b) 1, (c) 2 and (d) 3. Note that the Z-axis only goes from 15 to $23\,\mu$m (this is because the dipole used for CPP excitation is placed at $z = 0$).

the groove depth is still $\sim$300 nm). Considering the potential of CPP nanofocusing, further simulations are needed in order to elucidate the influence of all parameters (i.e. the initial groove angle and waveguide parameter) on the resulting effect of field enhancement.

5. Conclusions

In conclusion, we have investigated radiation nanofocusing with CPPs propagating along subwavelength metal grooves that are tapered synchronously in width and/or in depth. Efficient CPPs nanofocusing at telecom wavelengths with the field intensity enhancement of up to $\sim$130 for optimal taper configurations is directly demonstrated using near-field microscopy. Experimental observations are found concurrent with electromagnetic 3D-FDTD simulations, predicting the possibility of reaching the intensity enhancements of $\sim$1200 and opening thereby exciting perspectives for practical applications of CPP nanofocusing. One can envisage further developments of this concept for other plasmonic waveguides based on gap SP modes as well as with respect to applications for miniature biosensors by advantageously exploiting the fact the CPP-based nanophotonic circuits have been found to be performing exceptionally well [1, 19], for example by using consecutive Y-splitters for multichannel nanofocusing [17].

IOP Institute of Physics ⓓ DEUTSCHE PHYSIKALISCHE GESELLSCHAFT

References

[1] Ebbesen T W, Genet C and Bozhevolnyi S I 2008 Surface plasmon circuitry *Phys. Today* **61** 44–50

[2] Chang D E, Sørensen A S, Demler E A and Lukin M D 2007 A single-photon transistor using nanoscale surface plasmons *Nat. Phys.* **3** 807–12

[3] Fang N, Lee H, Sun C and Zhang X 2005 Sub-diffraction-limited optical imaging with a silver superlens, *Science* **308** 534–47

[4] Janunts N A, Baghdasaryan K S, Nerkararyan Kh V and Hech B 2005 Excitation and superfocusing of surface plasmon polaritons on a silver-coated optical fiber tip *Opt. Commun.* **253** 118–24

[5] Wang Y, Srituravanich W, Sun C and Zhang X 2008 Plasmonic nearfield scanning probe with high transmission *Nano Lett.* **8** 3041–5

[6] Ringler M, Schwemer A, Wunderlich M, Nichtl A, Kurzinger K, Klar T A and Feldmann J 2008 Shaping emission spectra of fluorescent molecules with single plasmonic nanoresonators *Phys. Rev. Lett.* **100** 203002

[7] Nerkararyan K V 1997 Superfocusing of a surface polariton in a wedge-like structure *Phys. Lett.* A **237** 103–5

[8] Gramotnev D K 2005 Adiabatic nanofocusing of plasmons by sharp metallic grooves: geometrical optics approach *J. Appl. Phys.* **98** 104302

[9] Vernon K C, Gramotnev D K and Pile D F P 2007 Adiabatic nanofocusing of plasmons by a sharp metal wedge on a dielectric substrate *J. Appl. Phys.* **101** 104312

[10] Stockman M I 2004 Nanofocusing of optical energy in tapered plasmonic waveguides *Phys. Rev. Lett.* **93** 137404

[11] Babadjanyan A J, Margaryan N L and Nerkararyan K V 2000 Superfocusing of surface polaritons in the conical structure *J. Appl. Phys.* **87** 3785–8

[12] Moreno E, Rodrigo S G, Bozhevolnyi S I, Martın-Moreno L and Garcıa-Vidal F J 2008 Guiding and focusing of electromagnetic fields with wedge plasmon polaritons *Phys. Rev. Lett.* **100** 023901

[13] Yang R, Abushagur M A G and Lu Z 2008 Efficiently squeezing near infrared light into a 24 nm-by-24 nm nanospot *Opt. Express* **16** 21042–8

[14] Verhagen E, Spasenović M, Polman A and Kuipers L K 2009 Nanowire plasmon excitation by adiabatic mode transformation *Phys. Rev. Lett.* **102** 203904

[15] Ropers C, Neacsu C C, Elsaesser T, Albrecht M, Raschke M B and Lienau C 2007 Grating-coupling of surface plasmons onto metallic tips: a nanoconfined light source *Nano Lett.* **7** 2784–8

[16] Verhagen E, Polman A and Kuipers L 2008 Enhanced nonlinear optical effects with a tapered plasmonic waveguide *Opt. Express* **16** 45–57

[17] Volkov V S, Bozhevolnyi S I, Rodrigo S G, Martín-Moreno L, García-Vidal F J, Devaux E and Ebbesen T W 2009 Nanofocusing with channel plasmon polaritons *Nano Lett.* **9** 1278–82

[18] Lu J Q and Maradudin A A 1990 Channel plasmons *Phys. Rev.* B **42** 11159

[19] Bozhevolnyi S I, Volkov V S, Devaux E, Laluet J-Y and Ebbesen T W 2006 Channel plasmon subwavelength waveguide components including interferometers and ring resonators *Nature* **440** 508

[20] Raether H 1988 *Surface Plasmons* (Berlin: Springer)

[21] Economou E N 1969 Surface plasmons in thin films *Phys. Rev.* **182** 539–54

[22] Choi H, Pile D F P, Nam S, Bartal G and Zhang X 2009 Compressing surface plasmons for nano-scale optical focusing *Opt. Express* **17** 7519

[23] Pfeiffer C A, Economou E N and Ngai K L 1974 Surface polaritons in a circularly cylindrical interface: surface plasmons *Phys. Rev.* B **10** 3038–51

[24] Takahara J, Yamagishi S, Taki H, Morimoto A and Kobayashi T 1997 Guiding of a one-dimensional optical beam with nanometer diameter *Opt. Lett.* **22** 475–7

[25] Ding W, Andrews S R and Maier S. A. 2007 Internal excitation and superfocusing of surface plasmon polaritons on a silver-coated optical fiber tip *Phys. Rev.* A **75** 063822

IOP Institute of Physics Φ DEUTSCHE PHYSIKALISCHE GESELLSCHAFT

[26] Gramotnev D K, Vogel M W and Stockman M I 2008 Optimized nonadiabatic nanofocusing of plasmons by tapered metal rods *J. Appl. Phys.* **104** 034311

[27] Moreno E, García-Vidal F J, Rodrigo S G, Martín-Moreno L and Bozhevolnyi S I 2006 Channel plasmon-polaritons: modal shape, dispersion, and losses *Opt. Lett.* **31** 3447–9

[28] Bozhevolnyi S I and Jung J 2008 Scaling for gap plasmon based waveguides *Opt. Express* **16** 2676–84

[29] Novikov I V and Maradudin A A 2002 Channel polaritons *Phys. Rev.* B **66** 035403

[30] Pile D F P and Gramotnev D K 2004 Channel plasmon-polariton in a triangular groove on a metal surface *Opt. Lett.* **29** 1069

[31] Gramotnev D K and Pile D F P 2004 Single-mode sub-wavelength waveguide with channel plasmon-polaritons in triangular grooves on a metal surface *Appl. Phys. Lett.* **85** 6323–5

[32] Pile D F P and Gramotnev D K 2005 Plasmonic subwavelength waveguides: next to zero losses at sharp bends *Opt. Lett.* **30** 1186–8

[33] Kaminow I P, Mammel W L and Weber H P 1974 Metal-clad optical waveguides: analytical and experimental study *Appl. Opt.* **13** 396–405

[34] Tanaka K and Tanaka M 2003 Simulations of nanometric optical circuits based on surface plasmon polariton gap waveguide *Appl. Phys. Lett.* **82** 1158–60

[35] Bozhevolnyi S I, Volkov V S, Devaux E and Ebbesen T W 2005 Plasmon-polariton guiding by subwavelength metal grooves *Phys. Rev. Lett.* **95** 046802

[36] Bozhevolnyi S I, Volkov V S, Devaux E, Laluet J-Y and Ebbesen T W 2007 Channelling surface plasmons *Appl. Phys. A: Mater. Sci. Process.* **89** 225–31

[37] Bozhevolnyi S I 2006 Effective-index modeling of channel plasmon polaritons *Opt. Express* **14** 9467–76

[38] Kogelnik H and Ramaswamy V 1974 Scaling rules for thin-film optical waveguides *Appl.Opt.* **13** 1857–62

[39] Bozhevolnyi S I and Nerkararyan K V 2009 Channel plasmon polaritons guided by graded gaps: closed-form solutions *Opt. Express* **17** 10327–34

[40] Volkov V S, Bozhevolnyi S I, Borel P I, Frandsen L H and Kristensen M 2005 Near-field characterization of low-loss photonic crystal waveguides *Phys. Rev.* B **72** 035118

[41] Radko I P, Bozhevolnyi S I and Gregersen N 2006 Transfer function and near-field detection of evanescent waves *Appl. Opt.* **45** 4054–61

[42] Bozhevolnyi S I, Vohnsen B and Bozhevolnaya E A 1999 Transfer functions in collection scanning near field optical microscopy *Opt. Commun.* **172** 171–9

[43] Taflove A and Hagness S C 2005 *Computational Electrodynamics: The Finite-Difference Time-Domain Method* 3rd edn (Boston, MA: Artech House)